The Planetary Science Journal, 4:30 (13pp), 2023 February https://doi.org/10.3847/PSJ/acab03

Reaction between Hydrogen and Ferrous/Ferric Oxides at High Pressures and High Temperatures—Implications for Sub-Neptunes and Super-Earths

H. W. Horn[1,2], V. Prakapenka[3], S. Chariton[3], S. Speziale[4], and S.-H. Shim[1]
[1] School of Earth and Space Exploration, Arizona State University, Tempe, AZ 85287, USA; hallensu@asu.edu, sshim5@asu.edu
[2] (current) Lawrence Livermore National Laboratory, Livermore, CA 94550, USA
[3] GeoSoilEnviroCARS, University of Chicago, Chicago, IL 60637, USA
[4] GFZ German Research Centre for Geosciences, Telegrafenberg, D-14473 Potsdam, Germany
Received 2022 February 25; revised 2022 November 3; accepted 2022 November 25; published 2023 February 13

Abstract

Sub-Neptune exoplanets may have thick hydrogen envelopes and therefore develop a high-pressure interface between hydrogen and the underlying silicates/metals. Some sub-Neptunes may convert to super-Earths via massive gas loss. If hydrogen chemically reacts with oxides and metals at high pressures and temperatures ($P-T$), it could impact the structure and composition of the cores and atmospheres of sub-Neptunes and super-Earths. While H_2 gas is a strong reducing agent at low pressures, the behavior of hydrogen is unknown at the $P-T$ expected for sub-Neptunes' interiors, where hydrogen is a dense supercritical fluid. Here we report experimental results of reactions between ferrous/ferric oxides and hydrogen at 20–40 GPa and 1000–4000 K utilizing the pulsed laser-heated diamond-anvil cell combined with synchrotron X-ray diffraction. Under these conditions, hydrogen spontaneously strips iron off the oxides, forming Fe-H alloys and releasing oxygen to the hydrogen medium. In a planetary context where this reaction may occur, the Fe-H alloy may sink to the metallic part of the core, while released oxygen may stabilize as water in the silicate layer, providing a mechanism to ingas hydrogen to the deep interiors of sub-Neptunes. Water produced from the redox reaction can also partition to the atmosphere of sub-Neptunes, which has important implications for understanding the composition of their atmospheres. In addition, super-Earths converted from sub-Neptunes may contain a large amount of hydrogen and water in their interiors (at least a few wt% H_2O). This is distinct from smaller rocky planets, which were formed relatively dry (likely a few hundredths wt% H_2O).

Unified Astronomy Thesaurus concepts: Planetary science (1255); Planet formation (1241); Exoplanet evolution (491); Exoplanets (498); Exoplanet formation (492); Planetary interior (1248)

1. Introduction

A large number of exoplanets have been discovered at sizes between Earth and Neptune (3.8 Earth radii, $R_\oplus$) from the Kepler mission (Bean et al. 2021). Demographics of these close-in orbiting exoplanets show some important features. For example, a much smaller number of planets have been found at 1.5–2.0 $R_\oplus$, which is called the "radius gap" (Fulton et al. 2017; Fulton & Petigura 2018). The gap appears to divide the exoplanets into low-density, larger-sized planets with thick atmospheres, called sub-Neptunes, and higher-density, smaller-sized planets with thin atmospheres, called super-Earths. The data set also reveals that the planets of 2.7–3 $R_\oplus$ size are 4–10× more abundant than planets just 20% larger, a phenomenon known colloquially as the "radius cliff" (Fulton & Petigura 2018; Kite et al. 2019).

These features in demographics are likely linked to the formation and evolution of these planets (Bean et al. 2021). In particular, sub-Neptune-type planets, with rocky/metallic cores and H-rich atmospheres, do not exist in our solar system, and therefore explaining their formation and evolution is an important challenge in planetary science (note that "core" in this paper refers to a dense heavy-element layer with silicates/oxides and metals following the sub-Neptune literature, rather than the metallic core at the center of rocky planets generally discussed in the rocky planet literature). As planets grow appreciably larger than Earth, their increased mass allows them to more efficiently accrete and retain nebular gas (Pollack et al. 1996). However, the noticeably smaller population of planets greater than 3 $R_\oplus$ (radius cliff) requires some other processes to explain the observation (Kite et al. 2019). Studies have shown that sub-Neptunes at $2 \leqslant R_\oplus \leqslant 3$ have likely interiors with the silicate/metal core overlaid by a thick hydrogen-dominated envelope (e.g., Rogers et al. 2011). Based on extrapolation of low-pressure experimental data from Hirschmann et al. (2012), Kite et al. (2019) suggest that the radius cliff is due to the increasing solubility of H_2 into the magma ocean (molten core) at pressures greater than a few gigapascals. Said pressure conditions can be achieved at the atmosphere−core interface of sub-Neptunes that reach 3 $R_\oplus$ while undergoing runaway accretion of nebular gas. Such ingassing could prevent further growth of H atmosphere and therefore increase in radius of the planets, possibly explaining the lower abundance of planets with >3 $R_\oplus$.

It is important to consider that hydrogen is a strong reducing agent. At 1 bar and 1000 K, FeO can be reduced to Fe metal by gaseous hydrogen, and the reaction produces H_2O (Sabat et al. 2014):

$$\text{FeO (oxide)} + \text{H}_2\text{ (gas)} \rightarrow \text{Fe (metal)} + \text{H}_2\text{O (vapor)}. \quad (1)$$

The Gibbs free energy for this reaction is 12.328 kJ mol^{-1} O_2, and therefore the reaction is endothermic. The kinetic effects for the reaction reduce with an increase in temperature and

become very small when FeO is molten at 1 bar (Chipman & Marshall 1940; Hayashi & Iguchi 1994).

If reaction 1 continues to occur at higher pressures, it will play an important role for the structure and evolution of sub-Neptunes. For example, the reaction could enable chemical exchange between the core and the atmosphere of sub-Neptunes. In addition, water can be produced and partition into atmosphere and core. Despite the importance, to our knowledge there are no experimental data examining the possibility of reaction 1 at the $P-T$ conditions estimated for the interface between a hydrogen-rich atmosphere and magma ocean (or the solid silicate/metal core) of sub-Neptunes and the upper part of magma oceans where hydrogen is physically mixed with silicate (pressures between a few to a few tens of gigapascals and temperatures over silicate melting, >2000 K; Stokl et al. 2016; Vazan et al. 2018). Under those conditions, hydrogen is a dense molecular fluid, not a gas (Trachenko et al. 2014), and H_2O is a dense molecular ionic fluid, not a vapor (Prakapenka et al. 2021), which can affect the energetics of reaction 1. For example, the reaction becomes strongly exothermic if H is an atomic gas instead of molecular gas at 1 bar and 1000 K (Sabat et al. 2014). It is also of interest whether a similar reduction by hydrogen can occur for Mg^{2+}, the main cation of planetary silicates/oxides. The Gibbs free energy of the $MgO + H_2 \rightarrow Mg + H_2O$ reaction decreases dramatically from $284.092\,kJ\,mol^{-1}\,O_2$ (endothermic) to $-15.632\,kJ\,mol^{-1}\,O_2$ (exothermic) at 1 bar and 1000 K if atomic hydrogen (2H) is considered instead of molecular hydrogen (H_2) (Sabat et al. 2014). However, there are no experimental results examining such chemical reactions at high $P-T$.

The main reason for the lack of such data are the difficulties working with hydrogen at high pressure (Deemyad et al. 2005). Being the smallest atom, hydrogen can diffuse into diamond anvils and make them extremely brittle, resulting in anvil damage or break. The problem becomes even more severe with laser heating. Technical advancements such as pulsed laser heating (Deemyad et al. 2005; Goncharov et al. 2010) and inert gasket coatings (Pepin et al. 2014) enable us to perform experiments at elevated $P-T$ conditions. In this work, we experimentally explore the possibility of iron-bearing oxides interacting with hydrogen at the $P-T$ conditions expected for the hydrogen-oxide/metal interface in sub-Neptunes. We also discuss implications of this interaction on sub-Neptunes.

2. Materials and Methods

2.1. Materials

Fe_2O_3 and MgO were 99.9% and 99.95% pure synthetic powders from Alfa Aesar, respectively. Fe metal was a 99.9% pure powder from Aldrich. $(Mg_{0.5}Fe_{0.5})O$ was synthesized at ambient pressure by wet chemistry producing a mixed (Mg,Fe) oxalate and then decomposed at 1100 K under an $f_{O_2} = 10^{-17}$ atmosphere for 10 hr. $(Mg_{0.9}Fe_{0.1})O$ was prepared by reaction of Fe_2O_3 with MgO and Fe in an Fe crucible at 1300 K for 10 hr in an evacuated silica tube. The powder was cold-pressed into foils with approximately 10 μm of thickness. All the samples were loaded without mixing with metallic Fe except for the MgO runs because MgO does not directly couple with near-IR lasers. The foils were loaded into a 125 μm hole drilled in a rhenium gasket that had been indented by diamond anvils with 200 μm diameter culets and then coated with ~800 Å of gold before sample loading, in order to prevent hydrogen diffusion into the gasket material. Spacer grains of the sample material were placed above and below the sample to provide thermal insulation from the diamond anvils during heating (Figure A1). Small grains of ruby and gold were loaded at the edge of the sample chamber away from the sample foil for pressure calibration during gas loading and synchrotron experiments, respectively. The cells were then placed in a Sanchez GLS 1500 gas loading system and then closed inside a chamber loaded with pure H_2 gas at a pressure of 1000–1500 bars. The samples were compressed to pressures between 20 and 40 GPa at 300 K before synchrotron laser heating experiments.

2.2. Synchrotron Experiments

Synchrotron X-ray diffraction (XRD) images were collected at high $P-T$ in the double-sided laser-heated diamond-anvil cell (LHDAC) at the 13-IDD beamline of the GeoSoilEnviroConsortium for Advanced Radiation Sources (GSECARS) sector at the Advanced Photon Source (APS). Monochromatic X-ray beams of wavelength 0.4133 Å or 0.3344 Å were focused on the sample in LHDAC. Near-infrared laser beams were coaxially aligned and focused with the X-ray beams for in situ laser heating. To reduce the amount of hydrogen diffusion into the anvils and the gasket material, we utilized the pulsed laser heating system at the GSECARS 13ID-D beamline at the APS (Deemyad et al. 2005; Goncharov et al. 2010). "Heating events" consisted of 10^5 pulses at 10 kHz. This gives a time of 10 s for each heating event, but the pulse width of 1 μs gives an integrated laser exposure time of 0.1 s. The laser heating spot size is approximately a 25 μm diameter circle, and the X-ray spot size is 3×4 μm. The heating events were synchronized with gated synchrotron X-ray beams such that diffraction measurements can take place only when the sample reaches the highest temperature during heating. Multiple heating events were conducted to accumulate enough diffraction peak intensities from the sample during high-temperature heating. The X-ray beam was coaxially aligned with the laser beams in order to obtain diffraction patterns at the center of the hot spot. The sufficiently smaller X-ray beam size also reduces the impact from radial thermal gradients in the hot spot. Previous studies have shown that the laser heating system provides a flat-top laser beam intensity profile, which is useful to further reduce thermal gradients in the hot spot (Prakapenka et al. 2008). We note that even though X-ray diffraction was measured only when the sample was heated by laser pulses, the temperature fluctuation between pulses is expected to be larger than that of continuous-wave laser heating. However, hydrogen diffuses into diamond anvils during continuous-wave laser heating. Therefore, continuous-wave laser heating cannot achieve a molten state for oxides in dense hydrogen fluid, which is the goal of this study. Instead, pulsed heating enabled us to achieve such conditions. While this method does produce larger temperature uncertainties, the temporal fluctuation was typically <200 K, within the stability field of oxide melt, which is sufficient for the goal of this study (the reaction between oxide melt and dense hydrogen fluid).

Temperatures were estimated by fitting thermal spectra from both sides to the graybody equation (Prakapenka et al. 2008). 2D diffraction images, collected from a Dectris Pilatus 1M CdTe detector, were integrated into 1D diffraction patterns using DIOPTAS (Prescher & Prakapenka 2015). Using the CeO_2 and LaB_6 standards, we determined the sample-to-detector distance

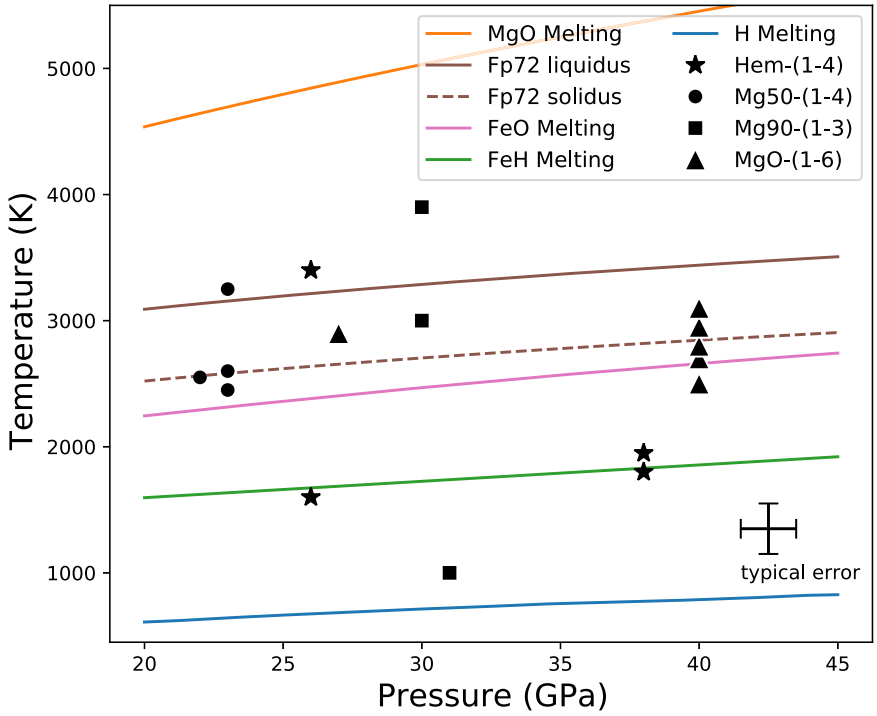

Figure 1. Pressure−temperature ($P-T$) conditions of the LHDAC experiments in this study (data points) shown with the melting curves of relevant materials: MgO (Kimura et al. 2017), $(Mg_{0.72}Fe_{0.28})O$ (Fu et al. 2018), FeO (Boehler 1992), FeH_x (Sakamaki et al. 2009), and H (Gregoryanz et al. 2003). No experiment in this study exceeded the melting temperature of MgO, while most were near or above the melting temperature of FeO and FeH_x. All experiments were conducted above the melting temperature of hydrogen.

and corrected for tilt of the detector. Pseudo-Voigt profile functions were fitted to the diffraction peaks to determine the unit-cell parameters in PeakPo (Shim 2022). The unit-cell parameter fitting was conducted based on the statistical approaches presented in Holland & Redfern (1997) in PeakPo. During synchrotron experiments, pressure was calculated by combining the measured unit-cell volume of gold with its equation of state (Ye et al. 2017) using Pytheos (Shim 2018). Pressure calibrants were placed at the edge of the sample chamber to avoid reactions/alloying with the sample material at high temperature, and thus pressure could not be measured during heating. Laser heating in a diamond-anvil cell can result in a pressure increase during heating (i.e., thermal pressure). Previous calculations have shown that thermal pressure of a liquid medium (Ar) at temperatures of 1000–4000 K is approximately 0.5–2.5 GPa (Dewaele et al. 1998). However, the pressure change is difficult to predict because it is sensitive to the properties of the medium used (Goncharov et al. 2007). The experiments presented here were conducted in a hydrogen medium, which is more compressible. Furthermore, the hydrogen medium around the heating spot should be fluid during heating, as the temperatures were well above the expected melting of hydrogen (Figure 1). Therefore, thermal pressure may not have been severe in our case. However, we assign a conservative estimate of 10% for the pressure uncertainty to reflect the fact that we did not measure pressure during laser heating.

3. Results

3.1. Fe_2O_3

At 38 GPa before heating, the ambient crystal structure of hematite (Blake et al. 1966) was distorted, causing the peak broadening seen in the diffraction pattern (Figure 2(a)) due to a combination of the stress of cold compression from 0 to 38 GPa (no thermal annealing) and the known distortion of the hematite structure culminating in a phase transition at ∼50 GPa (Rozenberg et al. 2002). It is also feasible that some amount of hydrogen may diffuse into the crystal structure of hematite, further distorting the structure. After a single heating event at 1500 K, all Fe_2O_3 peaks disappeared and Fe_2O_3 transformed into FeH_x and FeO through reaction with H (Figures 2(a) and (b)). FeH_x was in the face-centered cubic structure (fcc) as expected for these $P-T$ conditions (Pepin et al. 2014), which can be distinguished from fcc Fe by its significantly expanded unit-cell volume of 47.00 $Å^3$ at high pressure and 300 K after heating, in line with the expected unit-cell volume for stoichiometric ($x=1$) fcc FeH_x (Narygina et al. 2011), compared to the expected unit-cell volume of pure (hydrogen free) fcc Fe, 40.59 $Å^3$ (Figure A3; Boehler et al. 1990). Upon further heating (four more heating events) between 1600 and 2000 K, it transformed completely to fcc FeH_x, making it the sole phase remaining. All heating events occurred above the melting temperature of H_2 (Gregoryanz et al. 2003), below the melting temperature of FeO (Boehler 1992), and near the liquidus of FeH_x (Sakamaki et al. 2009; see Figure 1).

At 26 GPa, after a single heating event at 1300 K, Fe_2O_3 transformed into FeH_x and FeO through reaction with H, consistent with the experiment at 38 GPa. As in the higher-pressure experiments, the unit-cell expansion of the iron metal phase is consistent with stoichiometric fcc FeH_x with $x=1$ (Narygina et al. 2011). Upon further heating (five more heating events) between 1300 and 1600 K, it transformed completely to fcc FeH_x, making it the sole phase remaining. This observation is also consistent with the higher-pressure results. All heating events in this run (Hem-2) were conducted above the melting temperature of H but below the melting temperature of FeO (Figure 1). While FeO persisted, it maintained its cubic

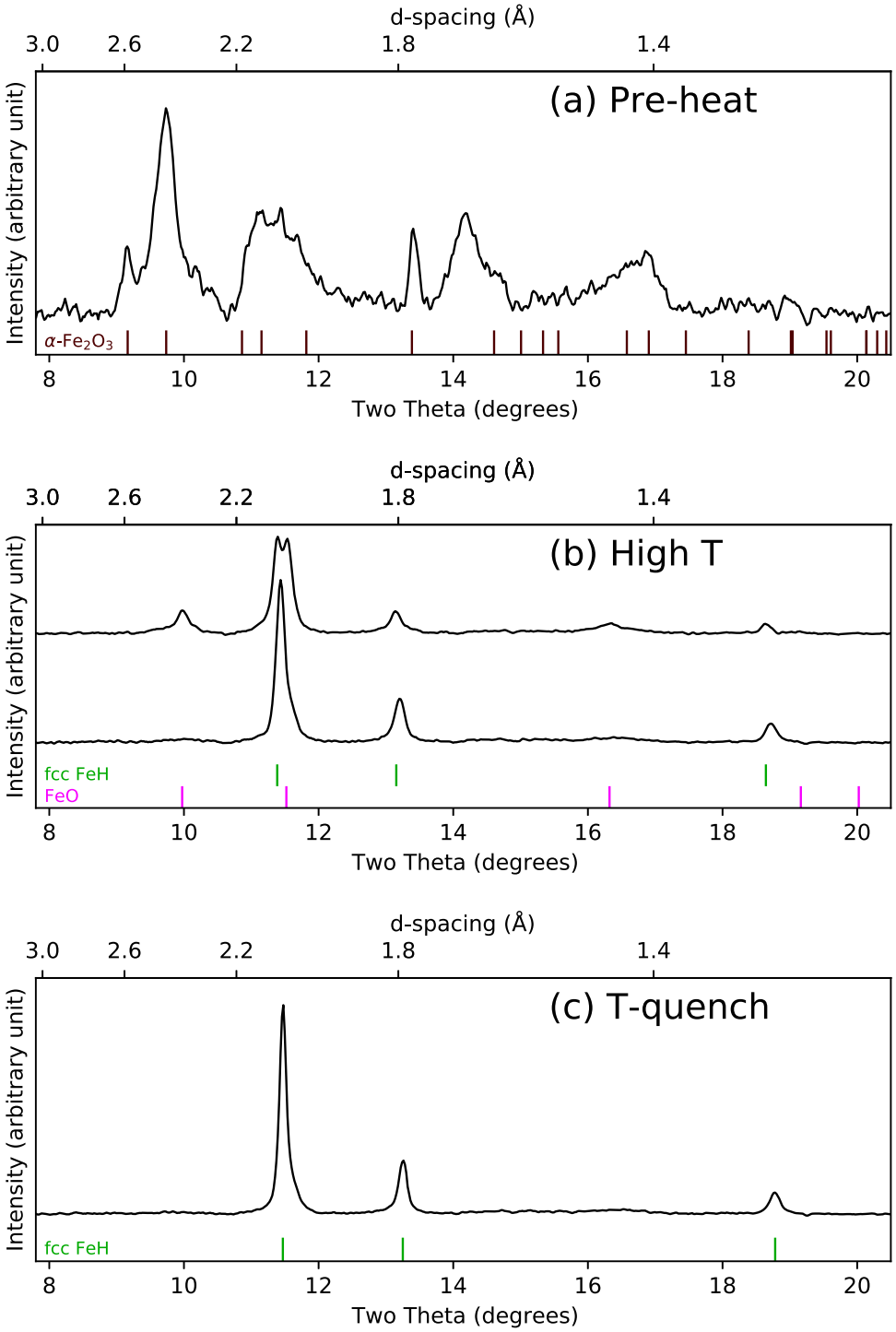

Figure 2. X-ray diffraction patterns from run Hem-4 (Table 1) taken at 38 GPa (a) before heating, (b) during heating (~1850 K), and (c) after heating. The upper pattern in panel (b) is during the first heating event, and the lower pattern is during the final heating event. The vertical tick marks below each integrated diffraction pattern represent the diffraction peak positions of the various observed mineral phases. Expected peak positions are calculated by combining the experimentally determined crystal structure and equation of state for a given material. Initially both FeO and FeH_x were formed, but after four heating events only FeH_x was observed in diffraction patterns.

structure at high temperatures, but it converted to the distorted rhombohedral structure (Yagi et al. 1985; Fei & Mao 1994; Ono et al. 2007) upon temperature quench to 300 K. However, experiment Hem-1 was conducted above the melting temperature of all materials involved and yielded the same results (although complete transformation of FeO to FeH_x was not achieved because heating was stopped after two events owing to the visible sign of the diamond anvils fracturing).

The XRD observations can be explained by the following chemical reaction:

$$Fe_2O_3 + 4H_2 \rightarrow 2FeO + H_2O + 3H_2 \rightarrow 2FeH + 3H_2O. \quad (2)$$

We have direct observation of diffraction peaks from Fe_2O_3, FeO, and FeH_x. The existence of H_2O is inferred from stoichiometry because it was difficult to unambiguously

identify the diffraction lines. The main diffraction peak of H_2O ice-VII (011) exists at nearly the same *d*-spacing (11.54°2θ) as the fcc FeH_x 111 reflection (11.43°2θ), as well as the FeO 200 reflection (11.63°2θ) at this pressure. Additionally, theoretical calculations have shown that H_2 (the pressure-transmitting medium in this study) and H_2O may be mutually miscible, particularly at high temperatures (Soubiran & Militzer 2015), thus possibly resulting in absence of H_2O ice-VII diffraction peaks. It is also notable that the X-ray scattering cross section of water is much smaller compared to iron-hydrogen alloy. The diamond anvils failed during the experiments, and therefore we could not decompress the sample for further X-ray diffraction or optical spectroscopy measurements.

3.2. Ferropericlase

3.2.1. $(Mg_{0.5}Fe_{0.5})O$

At 23 GPa, after laser heating at 2500–3200 K, XRD patterns showed diffraction peaks from FeH_x (Figure 3(a)). The observation suggests that H reduces Fe^{2+} in the (Mg,Fe)O starting material and induces the formation of iron-hydrogen alloy. This is supported by the fact that the unit-cell volume of the reacted ferropericlase was smaller than that of the starting $(Mg_{0.5}Fe_{0.5})O$ after laser heating at 300 K, shrinking to nearly that as expected for Fe-free MgO (see Figure A2). From the observations, we infer that no more than 10 mol% of Fe remains in the (Mg,Fe)O after laser heating in a H medium. Both the fcc and double hexagonal close-packed (dhcp) phases of iron-hydrogen alloy formed. The unit-cell volumes of the fcc and dhcp phases of FeH_x again suggest a 1:1 stoichiometry of iron and hydrogen (or $x \approx 1$), based on comparison with the previous reports (Figure A3; Narygina et al. 2011; Pepin et al. 2014). These XRD observations indicate

$$(Mg_{1-y}Fe_y)O + \frac{3}{2}yH_2 \rightarrow yFeH + (1-y)MgO + yH_2O, \quad (3)$$

where y is the amount of Fe^{2+} reduced from the oxide to FeH_x alloy. The reaction predicts formation of water, which can be supported by our observation of brucite, discussed later in this section.

The coexistence of the high-temperature phase fcc FeH_x (Narygina et al. 2011) and the low-temperature dhcp FeH_x phase (Badding et al. 1991) can likely be attributed to either thermal gradients during laser heating (Fiquet et al. 1996; Shen et al. 1998) or formation of the low-temperature phase upon temperature quenching (particularly from temperatures above the melting temperature of FeH_x). Though either possibility can explain this observation, the latter is supported by the fact that in experiment Hem-2, where heating was performed below the melting temperature of FeH_x, exclusively fcc FeH_x was observed despite the fact that the temperature was lower than the heating performed on all $(Mg_{0.5}Fe_{0.5})O$ samples where both the high-*T* fcc and low-*T* dhcp phases were observed. This is possible because during rapid temperature quenching fcc FeH_x forms at high temperature but does not fully crystallize before the temperature falls below the fcc–dhcp phase boundary. Once below that phase boundary, any remaining FeH_x crystallizes in the dhcp structure. Upon decompression to 1 bar, iron converts to the body-centered cubic (bcc) phase. The unit-cell parameter of the bcc phase, 2.865 ± 0.002 Å, matches well with the known value of 2.8667 Å (Rotter & Smith 1966), suggesting that no hydrogen or other elements persist in iron metal after pressure quench to ambient pressure (Figure A3).

Again, as in the experiments with Fe_2O_3, H_2O ice-VII was not unambiguously identified by XRD. This is again due to the peak overlaps with fcc FeH_x and/or MgO. It is also possibly due to the solubility of H_2O in the H medium as discussed in Section 3.1. However, in this case the system includes Mg, which remains oxidized as MgO. This is important because when temperature quenched MgO tends to react with H_2O to form $Mg(OH)_2$ brucite (via reaction 4) according to previous reports (Schmandt et al. 2014):

$$MgO + H_2O \rightarrow Mg(OH)_2. \quad (4)$$

Such a reaction consumes H_2O to form brucite, thus diminishing the diffraction intensity of H_2O-VII ice while enhancing the diffraction intensity of brucite. Indeed, after heating, there were sometimes a few weak diffraction spots in the diffraction images at high pressure well indexed with $Mg(OH)_2$ (brucite); however, its diffraction intensity was not high enough to appear in the integrated 1D diffraction patterns shown in Figure 3. Brucite cannot have formed at high temperature during heating because it decomposes at temperatures of 1000–1400 K in our pressure range (Fei & Mao 1993). Therefore, brucite should have formed during the temperature quench after heating or along the cooler rim of the heating spot at high pressure. This is confirmed by 2D XRD scan maps obtained at 1 bar and 300 K after the recovery of the sample (Figure 4). Ferropericlase detected at the hot spot (green circle in the figure) has the volume of MgO (Zigan & Rothbauer 1967), while ferropericlase outside the heated spot has the volume of $(Mg_{0.5}Fe_{0.5})O$. More Fe metal in the bcc structure, converted from FeH_x during decompression as found in previous studies (Badding et al. 1991), was detected at the hot spot. These two maps (Figures 4(a) and (b)) support the reduction of Fe^{2+} to FeH_x in a H medium at high *P*–*T*. In the diffraction mapping, brucite diffraction intensity is the strongest at the cooler rim surrounding the hottest heating center (Figure 4(c)). The brucite diffraction peaks became much stronger at 1 bar (Figure 3(b)). It has also been recently reported that MgO becomes soluble in H_2O at high *P*–*T* (Kim et al. 2021). In this case, they found that brucite appears during decompression or during temperature quench, as the solubility of MgO in H_2O decreases at lower pressures and lower temperatures. Laser heating is local, and therefore brucite likely precipitates first and more around the heated spot during temperature quench as found in Figure 4(c). Therefore, our observation can be interpreted as the result of the precipitation of brucite from Mg^{2+} dissolved in H_2O generated by the redox reaction (reaction 3).

3.2.2. $(Mg_{0.9}Fe_{0.1})O$

After one heating event at 1000 K (run Mg90-3; Table 1), strong diffraction peaks of brucite are present (Figure 3(c)). The observation is in contrast with Mg50 runs, where the temperature was too high for brucite formation at high pressure. There are also a few weak diffraction spots consistent with fcc FeH_x. In another run with this composition (Mg90-2), the temperature exceeded 4000 K. During this run, no brucite was formed. Instead, all that was observed after heating was

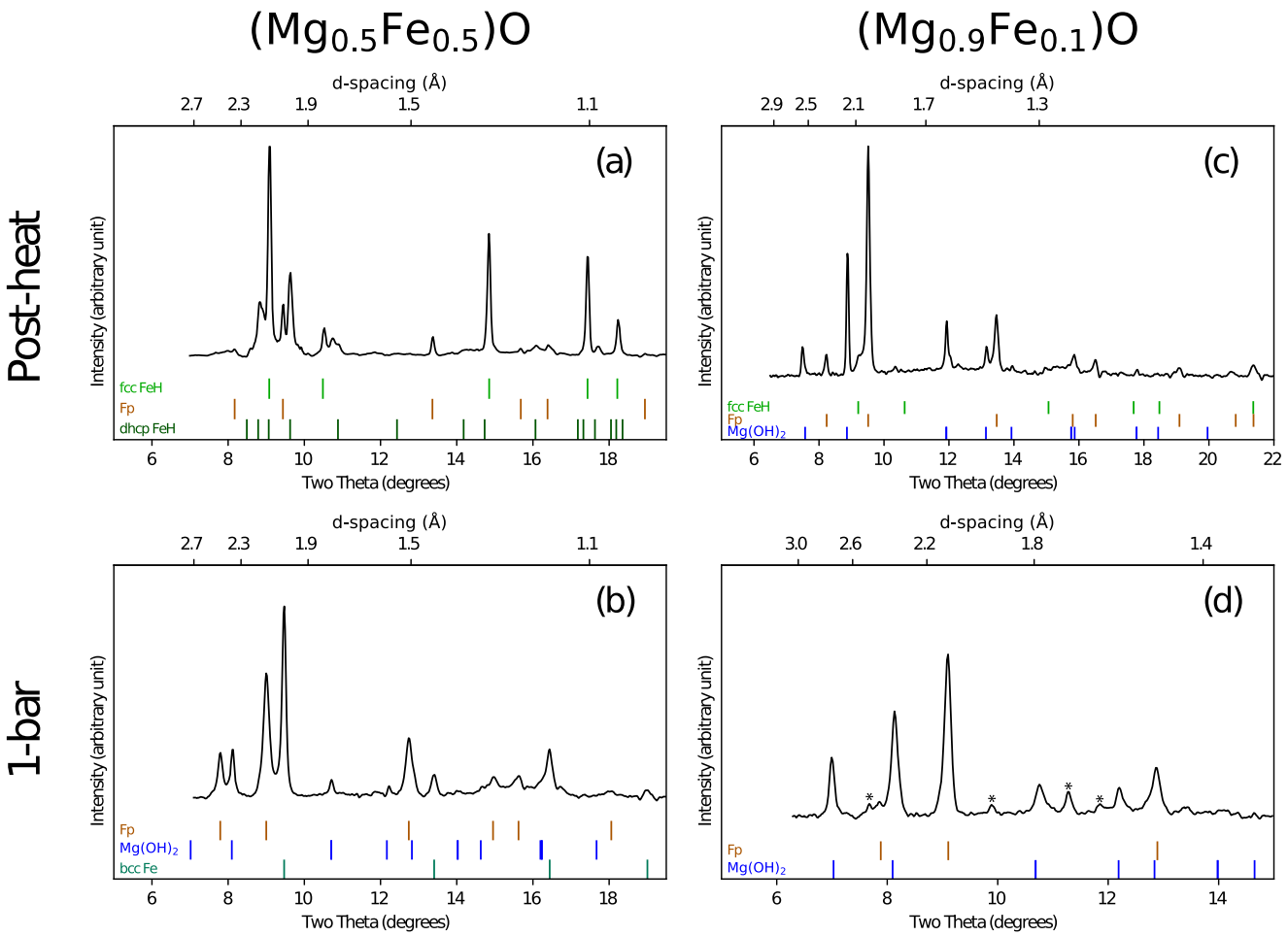

Figure 3. X-ray diffraction patterns showing temperature-quenched samples at high pressure after their final heating event (first row), and materials after decompression to 1 bar (second row). Patterns shown along columns and their respective heating temperatures are from experiments Mg50-2 (2450 K) and Mg90-1 (<1000 K) respectively (Table 1). Phases marked "Fp" represent any phase of composition $(Mg_{1-x}Fe_x)O$, as in many cases after heating the exact composition is unknown since the sample has reacted with hydrogen and lost some amount of Fe through reduction. The starred peaks in pattern (d) are unassigned. These peaks did not exist after heating at high pressure but appear when the sample was pressure quenched to 1 bar. Therefore, they are not related to the high-temperature reactions we focus on in this paper. They are likely from possible conversions of the sample during pressure unloading.

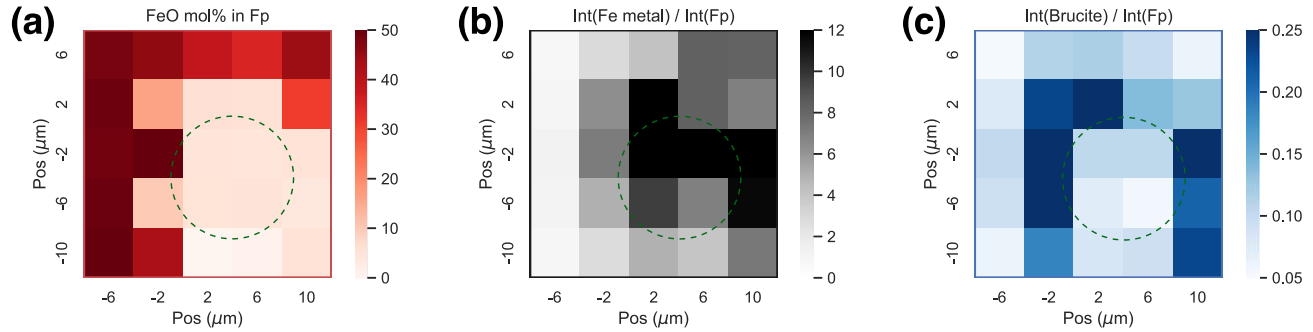

Figure 4. 2D X-ray diffraction map of the $(Mg_{0.5}Fe_{0.5})O$ sample heated in a pure H medium at 23 GPa and 2450 K. The mapping was conducted after the recovery of the sample at 1 bar and 300 K inside a diamond-anvil cell. The green dashed circle indicates the hot spot center. (a) Fe content in (Mg,Fe)O was calculated from the unit-cell volume using a linear relationship between the volume and the Fe content (Jackson & Rigden 1996). (b) Intensity ratio between Fe metal (bcc converted from FeH_x) and (Mg,Fe)O. (c) Intensity ratio between brucite and (Mg,Fe)O.

ferropericlase, with possibly a small amount of fcc and dhcp FeH_x. These results are consistent with those in the $(Mg_{0.5}Fe_{0.5})O$ experiments with two important differences, both of which can be attributed to the lower Fe concentration in the starting material. First, less FeH_x is observed owing to the simple fact that less Fe^{2+} is present in the starting material to be reduced to Fe metal. Second, at high pressure (30 GPa) more brucite was observed in this starting material than in the Mg50 experiments despite the fact that less Fe was present to reduce and release H_2O in $(Mg_{0.9}Fe_{0.1})O$ than in $(Mg_{0.5}Fe_{0.5})O$. This is because the lower Fe content facilitated less efficient laser coupling and therefore lower temperature heating in run Mg90-3 within the stability field of brucite (Fei & Mao 1993). However, in runs Mg90-1 and Mg90-2 such high laser power

Table 1
Experimental Runs Performed in This Study

Run #	S.M.	P (GPa)	T (K)	H.E.	Result
Hem-1	Fe_2O_3	26	3400 ± 200	2	FeO + fcc FeH_x
Hem-2	Fe_2O_3	26	1600 ± 300	6	fcc FeH_x
Hem-3	Fe_2O_3	38	2000 ± 1000	3	FeO + fcc FeH_x
Hem-4	Fe_2O_3	38	1850 ± 250	5	fcc FeH_x
Mg50-1	$(Mg_{0.5}Fe_{0.5})O$	23	3200 ± 400	4	(fcc+dhcp) FeH_x + $Mg(OH)_2$ + MgO
Mg50-2	$(Mg_{0.5}Fe_{0.5})O$	23	2450 ± 250	4	(fcc+dhcp) FeH_x + $Mg(OH)_2$ + MgO
Mg50-3	$(Mg_{0.5}Fe_{0.5})O$	22	2550 ± 500	2	(fcc+dhcp) FeH_x + MgO
Mg50-4	$(Mg_{0.5}Fe_{0.5})O$	23	2600 ± 200	2	dhcp FeH_x + MgO
Mg90-1	$(Mg_{0.9}Fe_{0.1})O$	30	3000 ± 350	2	fcc FeH_x + MgO + $Mg(OH)_2$
Mg90-2	$(Mg_{0.9}Fe_{0.1})O$	30	3900 ± 800	2	$(Mg_{0.9}Fe_{0.1})O$
Mg90-3	$(Mg_{0.9}Fe_{0.1})O$	31	<1000[a]	1	$Mg(OH)_2$ + fcc FeH_x + MgO
MgO-1	MgO + Fe	27	2900 ± 150	2	MgO + (fcc+dhcp) FeH_x
MgO-2	MgO + Fe	40	2700 ± 100	2	MgO + (fcc+dhcp) FeH_x
MgO-3	MgO + Fe	40	2800 ± 100	1	MgO + (fcc+dhcp) FeH_x
MgO-4	MgO + Fe	40	2500 ± 100	1	MgO + (fcc+dhcp) FeH_x
MgO-5	MgO + Fe	40	2950 ± 100	1	MgO + (fcc+dhcp) FeH_x
MgO-6	MgO + Fe	40	3100 ± 100	1	MgO + (fcc+dhcp) FeH_x

Notes. H.E.: number of heating events (10^5 laser pulses at 10 kHz; for more information, see Section 2.2). S.M.: starting material. Temperature, T, is given as the average T recorded from 20 measurements (10 each upstream and downstream) over 1 H.E., and the uncertainty is the standard deviation of those 20 measured temperatures. We estimate 10% uncertainty for the pressure values presented here (see related discussions in Section 2.2). fcc: face-centered cubic; dhcp: double hexagonal close-packed.
[a] Below detection threshold of the spectroradiometry.

was needed to achieve coupling that the temperature was very high, such that brucite cannot be stable at the heating center. As in the $(Mg_{0.5}Fe_{0.5})O$ runs, while the FeO component underwent melting, it is unlikely that the remaining MgO component underwent melting during heating.

In the diffraction patterns measured at 1 bar after pressure quench, some new diffraction peaks appeared, together with the peaks of (Mg,Fe)O and brucite (Figure 3(d)). The main unknown peak is at $d_{sp} = 1.703$ Å, with possible minor peaks at 1.602 and 1.940 Å (denoted with stars). The peaks could not be indexed with any expected iron or magnesium metal/hydride/hydroxide phases. We do not rule out a possibility of formation of a new Fe- or Mg-bearing phase (metal, hydride, or hydroxide) during decompression in the presence of H_2 and H_2O. The unit cell of ferropericlase was greater by about 0.5% than pure MgO, corresponding to ~7.5 mol% Fe, marginally less than the starting material (10 mol% Fe). For each mole of iron that is reduced from (Mg,Fe)O, 1 mole of H_2O is produced, which can then react with MgO to form brucite.

Little change in the Fe content of ferropericlase implies that nearly all H_2O produced reacted with MgO to form brucite. At 1 bar, brucite shows a ~1.3% smaller unit-cell volume than stoichiometric $Mg(OH)_2$ (Zigan & Rothbauer 1967; see Figure A4). At nanometer scale, thermally dehydrated brucite showed the existence of MgO layers, resulting in lower water content (Kumari et al. 2009). Although we do not have direct evidence, such a partially dehydrated form of brucite could have smaller unit-cell volume.

3.2.3. MgO

MgO was mixed with metallic iron, loaded with pure hydrogen, and compressed to target pressures (27 GPa for the discussions below; the MgO-1 run in Table 1). At high pressure before heating, iron metal was in the hydrogenated dhcp structure as previously reported (Badding et al. 1991). After heating to 2500–3000 K, no change was observed other than a few diffraction spots of fcc FeH_x formed from dhcp FeH_x, consistent with the formation of FeH_x structures from melt seen in the (Mg,Fe)O experiments. The transformation of iron to dhcp FeH_x and then fcc FeH_x with heating to higher temperatures is the expected behavior of the pure Fe-H binary system (Badding et al. 1991; Pepin et al. 2014; Umemoto & Hirose 2015). Upon decompression, FeH_x reverted to bcc Fe metal with a unit-cell parameter of 2.864 ± 0.002 Å, in agreement with the parameter for pure iron of 2.866 Å (Rotter & Smith 1966; Kohlhaas & Dunner 1967). We did not find any evidence of MgO reacting or interacting in any way with iron metal or hydrogen. The MgO unit-cell volume measured at ambient pressure after heating and decompression was 74.56 Å, consistent with the known value, 74.698 Å (Fiquet et al. 1996). This observation demonstrates that in the experiments with $(Mg_{1-x}Fe_x)O$ the formation of brucite was a secondary reaction between H_2O (produced by the reduction of FeO to FeH_x) and MgO (reaction 4), not a direct reaction between MgO and H_2.

4. Discussion

Our experiments have shown that dense molecular hydrogen fluid at pressures of 20–40 GPa and temperatures up to 4000 K reduces iron oxides to iron-hydrogen alloys and releases O (likely in the form of H_2O). From the phase diagrams, our $P-T$ conditions yielded FeO-rich partial melt from (Mg,Fe)O (Figure 1). Therefore, Fe metal may be formed from partial melt. FeH_x should form as melt and H_2O should form as dense ionic fluid at the $P-T$ conditions of our experiments. At the $P-T$ conditions expected for the interface between H envelope and oxide/metal core, and for the upper part of the magma ocean where H is dissolved (pressures between a few to a few tens of gigapascals and temperatures over silicate melting, >2000 K; Stokl et al. 2016; Vazan et al. 2018), the reaction will increase the amount of ingassed H_2 beyond the level in previous models (e.g., Kite et al. 2019), which assumed physical mixing of H_2 only (Figure 5). In addition, H_2O fluid

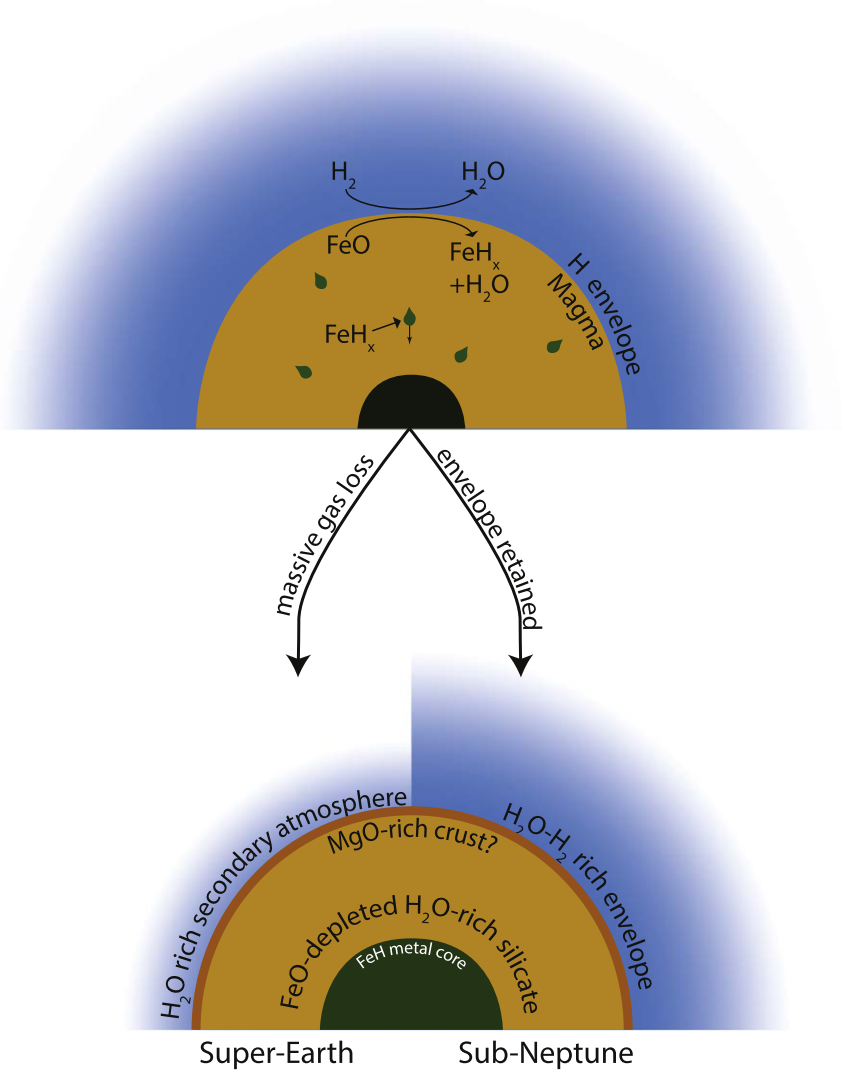

Figure 5. Cartoon demonstrating possible implications of the chemical reactions explored in this work. Of particular importance is the link between the atmosphere and interior showing that in large exoplanets the oxidation of the atmosphere may stem from the reduction of the interior. It also demonstrates how super-Earths formed through atmospheric loss from a sub-Neptune may retain significant amounts of their primordial hydrogen stored in the metal part of the core as an alloy component or the silicate part of the core as H_2O.

and silicate melt become miscible with each other at a few gigapascals of pressure (Stalder et al. 2001). Therefore, the H_2O produced from the redox reaction involving main components of magma, Fe in this case, can dissolve in the magma. We found no sign of reduction of Mg^{2+} to metal by hydrogen fluid. Therefore, after reaction with hydrogen, the rocky portion of the core will be deficient of FeO (or MgO rich).

Our experiments found brucite from the reaction between MgO and water. While brucite is unlikely to form during heating, it is instead likely formed during temperature or pressure quenching. Therefore, brucite would not exist in hot sub-Neptunes. Instead, its appearance indicates that H_2O can be incorporated as OH in the silicate-oxide part of sub-Neptunes' solid body. Our experiments show that H_2O produced from the reaction is not sufficient to affect the siderophile behavior of H and its alloying with Fe metal to produce FeH_x.

Water partitioned in the magma ocean would decrease the melting temperature (Litasov & Ohtani 2002) and therefore extend the magma ocean stage for the cores of sub-Neptunes. However, at the same time the removal of FeO from magma from reaction 1 would increase the relative amount of MgO, thus increasing the melting temperature of magma and hastening its solidification. If a FeO-depleted layer forms quickly at the topmost part of the oxide magma ocean where magma reacts with dense hydrogen fluid, it can crystallize and form solid crust, which could shut down reaction 3 and therefore limit the ingassing of H (Figure 5). However, such a process can be also affected by convectional vigor of the magma ocean system and the strength of the FeO-depleted ultramafic layer at high $P-T$, which requires further study.

Studies have suggested that the cores of the sub-Neptunes are dominantly silicates and metals (Rogers & Owen 2021). If all FeO is reduced to Fe metal and forms an alloy with H, assuming sufficient supply of hydrogen,

$$\mathrm{FeO} + 3\mathrm{H} \rightarrow \mathrm{FeH} + \mathrm{H_2O}. \quad (5)$$

Earth's mantle contains 7.60 wt% FeO according to the pyrolite model (Ringwood 1975). If all FeO is reduced, reaction 5 predicts formation of 7.64×10^{22} kg H_2O for the mass of Earth's mantle, 4.01×10^{24} kg. If all the H_2O produced in this way

remains in the magma ocean, the water content of the magma ocean is 2 wt%, which corresponds to 55 times the mass of Earth's ocean for Earth-like size and composition. Because H_2O can partition into the H atmosphere and metallic part of the core, this estimation should be regarded as the upper bound of H_2O content in the silicate part of the core. Reduction of FeO in silicate and conversion to FeH can increase the mass of the metallic part of the core. From reaction 5, reduction of all FeO in Earth's mantle produces 2.41×10^{23} kg FeH, which will increase the core mass by 12%, offsetting the mass loss of the silicate part (8%). From reaction 5, to reduce all FeO in Earth's mantle, 1.28×10^{22} kg of H is required, which is 0.22 wt% of the planet. Again, for the reasons we discussed above, this amount should be regarded as the upper bound. Therefore, the amount of ingassed hydrogen we discuss here is ~2 wt%, consistent with the view that the dominant components of the core of sub-Neptunes are mainly silicates and metals but not ice (Rogers & Owen 2021). In fact, the amount of ingassed hydrogen we discuss here is unlikely to be detectable from the analysis of the mass–radius data of exoplanets in current data sets considering the significant uncertainties involved in those properties. While the dissolved H would further enhance the reduction of FeO in the interiors of magma oceans of sub-Neptunes, the redox reaction alone does not ingass sufficient H (much less than 1 wt%) to explain the "radius cliff," which requires ingassing of at least 1.5 wt% H_2 (Kite et al. 2019). We note that estimation here is not intended to provide a detailed internal structure model for hydrogen-rich sub-Neptunes, particularly element distribution among different layers. For a detailed model, there are many other factors to consider. For example, experiments have shown that hydrogen partitions preferentially to metal over silicate melt at high pressures (Tagawa et al. 2021). Therefore, much H_2O dissolved in magma ocean by the redox reaction ultimately breaks down, and more hydrogen partitions into the metallic part of the core.

On the other hand, if a large amount of H_2 (>1.5 wt% H_2) can indeed be ingassed into the silicate/oxide magma ocean through physical mixing (Kite et al. 2019), the amount is enough to reduce all FeO for Earth-like and Mars-like compositions. One source of uncertainty for applying our results to sub-Neptunes is that the pressure in the deeper part of magma ocean is much higher than we studied in this paper. Above 100 GPa, hydrogen fluid undergoes a change from a molecular to a monoatomic form (Cheng et al. 2020). H_2O is likely an ionic fluid within the P–T range we studied here (Prakapenka et al. 2021) and likely at the $P-T$ conditions of sub-Neptunes' interface (Millot et al. 2019). However, H_2O could be a conducting fluid at pressures over 100 GPa (Prakapenka et al. 2021). FeO also undergoes a metallization transition at 50–70 GPa (Knittle & Jeanloz 1986; Fischer et al. 2011; Ohta et al. 2012), which is higher than our experimental conditions but overlaps with the transitions in behaviors of H_2O and H_2. Such a fundamental change in the properties of reactants and products in reaction 1 could change the behavior of the system. If such changes can lead to different redox behavior of the system in the core, it would have important implications for the storage of volatiles and the structure of the very deep interiors of larger sub-Neptunes, which should be considered in future modeling efforts.

To explain the "radius gap," models have suggested that the large loss of a thick hydrogen envelope of sub-Neptunes, through either photoevaporation (and migration) or core-powered loss, could result in a conversion to super-Earths (Owen & Wu 2013; Schlichting 2014; Bean et al. 2021). Our experiment shows that, through reduction of FeO and alloying of H and Fe, a large amount of hydrogen can be sequestered in the metallic part of the sub-Neptunes' core (because at least 1.8 wt% H can dissolve in Fe metal at high pressures; Badding et al. 1991). The dissolved H will remain in the metallic core of super-Earths after conversion because of the strong siderophilic behavior of H at high pressures (Tagawa et al. 2021). Our results also found that some H_2O produced by the reduction of FeO can hydrate the silicate/oxide part of the sub-Neptunes' cores. Therefore, from these, we can conclude that super-Earths converted from sub-Neptunes likely have interiors rich in water and/or hydrogen compared to Earth. With cooling of magma ocean, an MgO-rich crystalline layer could form at the topmost part while the deeper part may still be molten. If the structure can be preserved during gas loss, super-Earths converted from sub-Neptunes could have an ultramafic crust unlike Earth (Figure 5).

It is also interesting to point out that the cores of sub-Neptunes will experience a few to a few tens of gigapascals of pressure decrease during gas loss. The magnitude of the decrease is small compared with the very large pressure expected for the deep interiors of sub-Neptunes' (or super-Earths') cores. However, the topmost layer can be affected by such a pressure decrease. If the solubilities of H_2O and H_2 in silicate increase with pressure, the topmost layer could experience a loss of these volatiles during decompression. The released H_2O and H_2 could be incorporated into the atmosphere and ultimately removed during conversion to super-Earths (Figure 5). However, whether they can remain and form secondary atmosphere after the conversion to super-Earths or not is likely dependent on the rate of massive gas loss versus the rate of degassing from the interior, particularly if surface tectonics can control (or delay) the degassing. However, the H stored in the metallic core of former sub-Neptunes is unlikely to be affected by the massive gas loss, as the pressure decrease is not enough to change the alloying behavior of H at such high pressures, more than 1 Mbar.

If the water formed from the FeO reduction by hydrogen could be outgassed to form H_2O-rich secondary atmospheres (Kite & Schaefer 2021), it can provide a pathway for endogenic high molecular weight atmospheres without relying on delivery of solid-derived volatiles (Ikoma & Genda 2006). However, this does not mean to explain the oceans on Earth. Despite Earth's depletion of FeO and perceived deep reservoirs of nebular hydrogen (Genda & Ikoma 2008; Hallis et al. 2015; Wu et al. 2018), nearly 50 oceans of hydrogen would need to be reacted with FeO to explain the depletion, far exceeding even the most generous estimations for nebular gas interaction and hydrogen in the core. Instead, this reaction may play an important role in the formation of sub-Neptunes that grow large enough to accrete large primarily H-dominated envelopes.

It is important to point out that the formation of FeH_x alloy instead of Fe metal expected for sub-Neptunes as shown by experiments makes an important contrast for the composition of the metallic cores of super-Earths that are converted from sub-Neptunes as opposed to overgrown terrestrial planets. If a significant amount of H is ingassed through physical mixing,

sinking Fe metal blobs in the magma ocean can alloy with H, i.e., chemical ingassing. As H solubility in Fe metal increases with pressure (Pepin et al. 2017; Piet et al. 2021), such direct alloying of H to iron metal can result in large hydrogen ingassing to the cores of these larger planets. An interesting consequence would be that the larger rocky planets' metallic and oxide parts of the cores generally contain more hydrogen than smaller rocky planets. It is also likely that larger rocky planets' silicate mantle is depleted in FeO but rich in water and hydrogen, which could alter the viscosity and therefore impact the vigor of mantle convection and thermal evolution.

5. Conclusion

We found that at high pressure–temperature conditions relevant for the interface between H and the cores of sub-Neptunes iron-bearing oxides react with hot dense hydrogen to form iron-hydrogen alloys and water. The chemical sequestration of hydrogen as H_2O as a result of the reduction of FeO, as well as the subsequent formation of FeH_x, provides a chemical pathway to supplement physical mixing and enhance the solubility of H in a global magma ocean. Although physical mixing of H could still be important, these chemical reactions support the theory that the superabundance of sub-Neptunes can be explained by the sharp increase in H in the condensed planetary core as pressure at the base of the H envelope exceeds 10^9 Pa, whereby additional accreted H is partitioned to the interior rather than the atmosphere. These reactions also have implications for the chemical partitioning of growing large planets. Due to the significant amount of H that can alloy with molten Fe, metallic layers of cores on sub-Neptunes (or super-Earths that formed via atmospheric loss from sub-Neptunes) may be rich in H. Additionally, the formation of H_2O from the released oxygen may enrich mantles and atmospheres with water, even without direct delivery of H_2O-rich materials. In addition to the support for existing models of planet formation, the chemical reactions explored in this work provide valuable data to build future models and theories. A forthcoming follow-up paper will explore the effect of H on Si-bearing systems (Mg-Fe-Si-O-H), as well as lower pressures relevant to shallow magma oceans and magma ocean/envelope interfaces on early rocky planets.

S.-H.S and H.A.S were supported by National Aeronautics and Space Administration (NASA) grant 80NSSC18K0353 and National Science Foundation (NSF) grants AST-2108129 and EAR-1921298. Portions of this work were performed at GeoSoilEnviroCARS (The University of Chicago, Sector 13), Advanced Photon Source (APS), Argonne National Laboratory. GeoSoilEnviroCARS is supported by the National Science Foundation—Earth Sciences (EAR-1634415) and Department of Energy (DOE)—GeoSciences (DE-FG02-94ER14466). This research used resources of the Advanced Photon Source, a U.S. DOE Office of Science User Facility operated for the DOE Office of Science by Argonne National Laboratory under contract No. DE-AC02-06CH11357. We acknowledge the use of facilities within the Eyring Materials Center at ASU. This work was performed under the auspices of the U.S. Department of Energy by the Lawrence Livermore National Laboratory under contract DE-AC52-07NA27344. This document was prepared as an account of work sponsored by an agency of the United States government. Neither the United States government nor Lawrence Livermore National Security, LLC, nor any of their employees makes any warranty, expressed or implied, or assumes any legal liability or responsibility for the accuracy, completeness, or usefulness of any information, apparatus, product, or process disclosed, or represents that its use would not infringe privately owned rights. Reference herein to any specific commercial product, process, or service by trade name, trademark, manufacturer, or otherwise does not necessarily constitute or imply its endorsement, recommendation, or favoring by the United States government or Lawrence Livermore National Security, LLC. The views and opinions of authors expressed herein do not necessarily state or reflect those of the United States government or Lawrence Livermore National Security, LLC, and shall not be used for advertising or product endorsement purposes. The experimental data for this paper are available by contacting hallensu@asu.edu.

Appendix

Supplementary figures (Figures A1–A4).

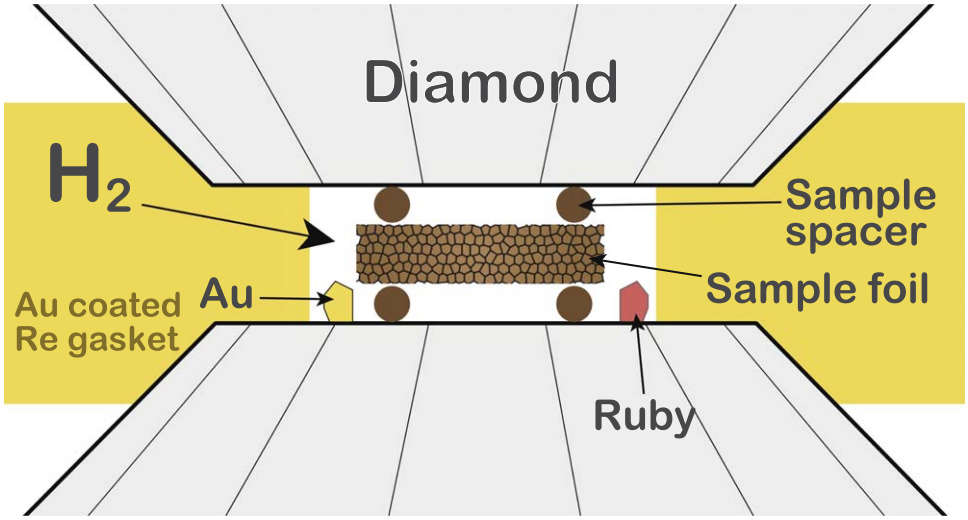

Figure A1. Schematic diagram of the sample loading in this study. Note that the sample spacers allow for hydrogen layers to form during gas loading. The hydrogen layers then insulate the sample foil from the diamond anvils. Particles of gold and ruby were placed to the side of the sample chamber to avoid sample contamination by potential chemical reaction.

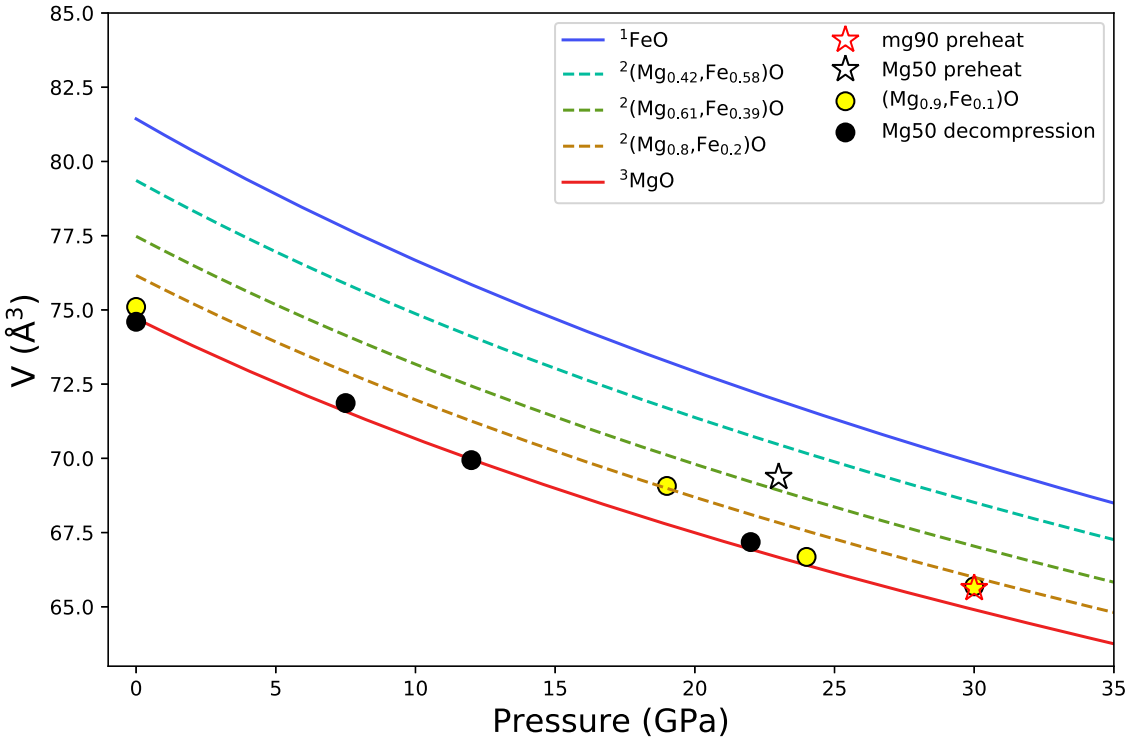

Figure A2. The unit-cell volume of ferropericlase before (stars) and after (circles) heating and subsequent decompression to 1 bar for heating runs Mg50-2 (black) and Mg90-1 (yellow). Also shown are compositional curves for the pressure–volume relationship of (Mg,Fe)O with various Fe contents: [1]FeO from Fischer et al. (2011), [2](Mg,Fe)O from Fei et al. (2007), and [3]MgO from Speziale et al. (2001).

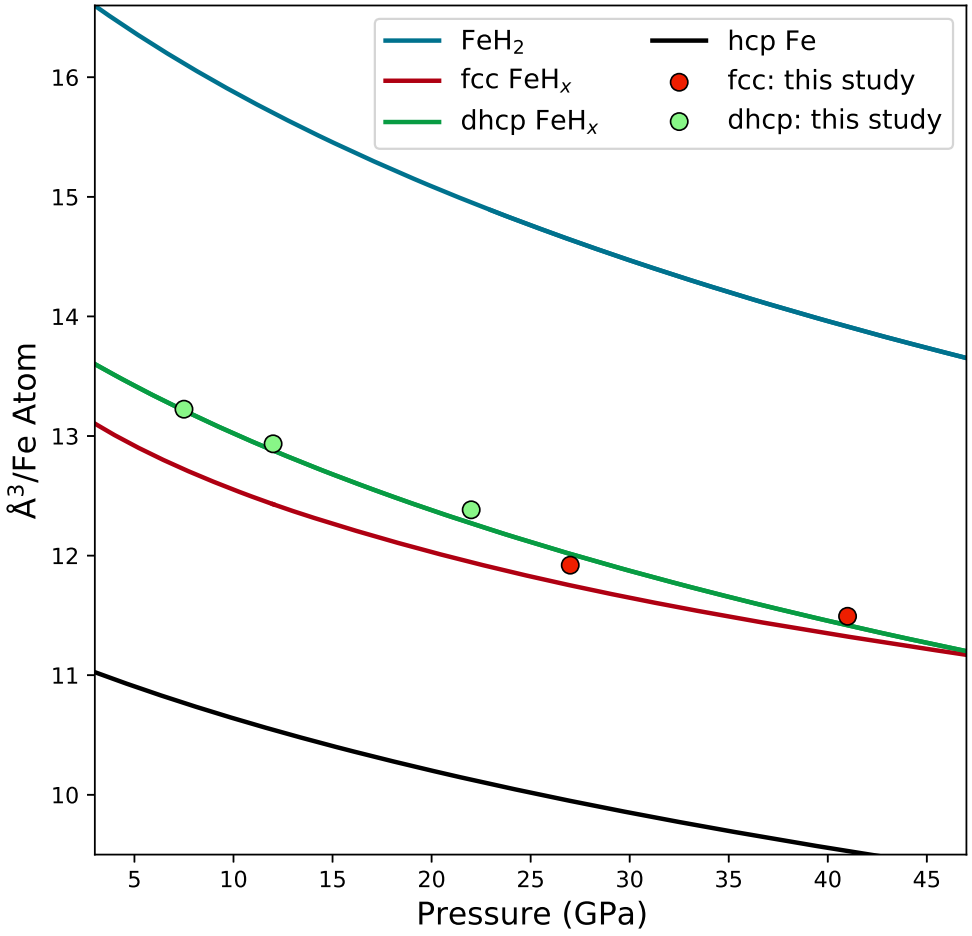

Figure A3. Comparison of the volumes per Fe atom (V/Z) of Fe and Fe-H phases observed in our experiments and the volume previously reported at 300 K. Both the fcc and dhcp FeH_x phases observed in this study (red and green circles, respectively) show V/Z consistent with 1:1 stoichiometric FeH (colored curves). Equations of state for hcp Fe, fcc FeH, dhcp FeH, and FeH_2 are from Dewaele et al. (2006), Narygina et al. (2011), Pepin et al. (2014), and Pepin et al. (2014), respectively.

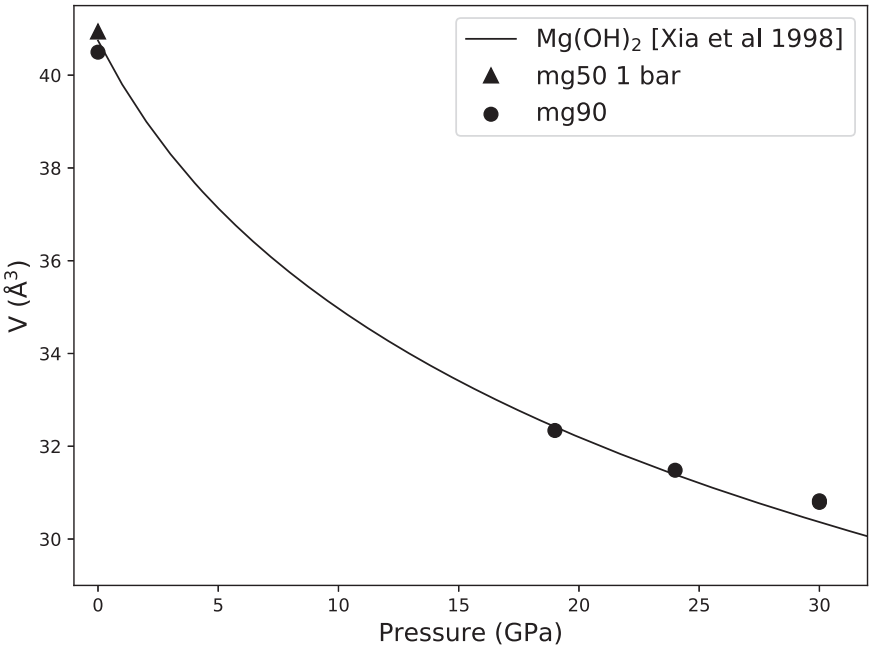

Figure A4. Pressure–volume data for brucite formed in run Mg90-3, along with the 1 bar measurement from run Mg50-2 (Table 1). The data points were measured at 300 K. We also show the equation of state from Xia et al. (2015) at 300 K for comparison.

ORCID iDs

H. W. Horn https://orcid.org/0000-0003-3809-0446
S.-H. Shim https://orcid.org/0000-0001-5203-6038

References

Badding, J., Hemley, R., & Mao, H. 1991, Sci, 253, 421
Bean, J. L., Raymond, S. N., & Owen, J. E. 2021, JGRE, 126, e06639
Blake, R., Hessevick, R., Zoltai, T., & Finger, L. W. 1966, AmMin, 51, 123
Boehler, R. 1992, E&PSL, 111, 217
Boehler, R., von Bargen, N., & Chopelas, A. 1990, JGR, 95, 21731
Cheng, B., Mazzola, G., Pickard, C. J., & Ceriotti, M. 2020, Natur, 585 217
Chipman, J., & Marshall, S. 1940, JAChS, 62, 299
Deemyad, S., Sterer, E., Barthel, C., et al. 2005, RScI, 76, 125104
Dewaele, A., Fiquet, G., & Gillet, P. 1998, RScI, 69, 2421
Dewaele, A., Loubeyre, P., Occelli, F., et al. 2006, PhRvL, 97, 215504
Fei, Y., & Mao, H.-K. 1993, JGR, 98, 11875
Fei, Y., & Mao, H.-k. 1994, Sci, 266, 1678
Fei, Y., Zhang, L., Corgne, A., et al. 2007, GeoRL, 34, L17307
Fiquet, G., Andrault, D., Itie, J. P., Gillet, P., & Richet, P. 1996, PEPI, 95, 1
Fischer, R. A., Campbell, A. J., Shofner, G. A., et al. 2011, E&PSL, 304, 496
Fu, S., Yang, J., Zhang, Y., et al. 2018, E&PSL, 503, 1
Fulton, B. J., & Petigura, E. A. 2018, AJ, 156, 264
Fulton, B. J., Petigura, E. A., Howard, A. W., et al. 2017, AJ, 154, 109
Genda, H., & Ikoma, M. 2008, Icar, 194, 42
Goncharov, A. F., Crowhurst, J. C., Dewhurst, J. K., et al. 2007, PhRvB, 75, 224114
Goncharov, A. F., Prakapenka, V. B., Struzhkin, V. V., et al. 2010, RScI, 81, 113902
Gregoryanz, E., Goncharov, A. F., Matsuishi, K., Mao, H.-k., & Hemley, R. J. 2003, PhRvL, 90, 175701
Hallis, L. J., Huss, G. R., Nagashima, K., et al. 2015, Sci, 350, 795
Hayashi, S., & Iguchi, Y. 1994, ISIJ international, 34, 555
Hirschmann, M. M., Withers, A., Ardia, P., & Foley, N. 2012, E&PSL, 345, 38
Holland, T. J. B., & Redfern, S. A. T. 1997, MinM, 61, 65
Ikoma, M., & Genda, H. 2006, ApJ, 648, 696
Jackson, I., & Rigden, S. M. 1996, PEPI, 96, 85
Kim, T., Chariton, S., Prakapenka, V., et al. 2021, NatAs, 5, 815
Kimura, T., Ohfuji, H., Nishi, M., & Irifune, T. 2017, NatCo, 8, 1
Kite, E. S., Fegley, B., Jr., Schaefer, L., & Ford, E. B. 2019, ApJL, 887, L33
Kite, E. S., & Schaefer, L. 2021, ApJL, 909, L22
Knittle, E., & Jeanloz, R. 1986, GeoRL, 13, 1541
Kohlhaas, R., & Dunner, P. 1967, ZAPhy, 23, 245
Kumari, L., Li, W. Z., Vannoy, C. H., Leblanc, R. M., & Wang, D. Z. 2009, Ceramics International, 35, 3355
Litasov, K., & Ohtani, E. 2002, PEPI, 134, 105
Millot, M., Coppari, F., Rygg, J. R., et al. 2019, Natur, 569, 251
Narygina, O., Dubrovinsky, L. S., McCammon, C. A., et al. 2011, E&PSL, 307, 409
Ohta, K., Cohen, R. E., Hirose, K., et al. 2012, PhRvL, 108, 026403
Ono, S., Ohishi, Y., & Kikegawa, T. 2007, JPCM, 19, 036205
Owen, J. E., & Wu, Y. 2013, ApJ, 775, 105
Pepin, C. M., Dewaele, A., Geneste, G., Loubeyre, P., & Mezouar, M. 2014, PhRvL, 113, 265504
Pepin, C. M., Geneste, G., Dewaele, A., Mezouar, M., & Loubeyre, P. 2017, Sci, 357, 382
Piet, H., Chizmeshya, A. V. G., Chen, B., et al. 2021, PhRvB, 104, 224106
Pollack, J. B., Hubickyj, O., Bodenheimer, P., et al. 1996, Icar, 124, 62
Prakapenka, V. B., Holtgrewe, N., Lobanov, S. S., & Goncharov, A. F. 2021, NatPh, 17, 1233
Prakapenka, V. B., Kubo, A., Kuznetsov, A., et al. 2008, HPR, 28, 225
Prescher, C., & Prakapenka, V. B. 2015, HPR, 35, 223
Ringwood, A. E. 1975, Composition and Petrology of the Earth's Mantle, 618 (New York: McGraw-Hill)
Rogers, J. G., & Owen, J. E. 2021, MNRAS, 503, 1526
Rogers, L. A., Bodenheimer, P., Lissauer, J. J., & Seager, S. 2011, ApJ, 738, 59
Rotter, C. A., & Smith, C. S. 1966, JPCS, 27, 197
Rozenberg, G. K., Dubrovinsky, L. S., Pasternak, M. P., et al. 2002, PhRvB, 65, 064112
Sabat, K. C., Rajput, P., Paramguru, R. K., Bhoi, B., & Mishra, B. K. 2014, Plasma Chemistry and Plasma Processing, 34, 1
Sakamaki, K., Takahashi, E., Nakajima, Y., et al. 2009, PEPI, 174, 192
Schlichting, H. E. 2014, ApJL, 795, L15
Schmandt, B., Jacobsen, S. D., Becker, T. W., Liu, Z., & Dueker, K. G. 2014, Sci, 344, 1265
Shen, G., Mao, H.-k., Hemley, R. J., Duffy, T. S., & Rivers, M. L. 1998, GeoRL, 25, 373
Shim, S.-H. 2018, Pytheos—a python tool set for equations of state, doi:10.5281/zenodo.344973
Shim, S.-H. 2022, SHDShim/PeakPo: Include support for producing executables (7.7.34), Zenodo, doi:10.5281/zenodo.6640493
Soubiran, F., & Militzer, B. 2015, ApJ, 806, 228
Speziale, S., Zha, C.-S., Duffy, T. S., Hemley, R. J., & Mao, H.-K. 2001, JGR, 106, 515
Stalder, R., Ulmer, P., Thompson, A., & Gunther, D. 2001, CoMP, 140, 607
Stokl, A., Dorfi, E. A., Johnstone, C. P., & Lammer, H. 2016, ApJ, 825, 86
Tagawa, S., Sakamoto, N., Hirose, K., et al. 2021, NatCo, 12, 1
Trachenko, K., Brazhkin, V. V., & Bolmatov, D. 2014, PhRvE, 89, 032126
Umemoto, K., & Hirose, K. 2015, GeoRL, 42, 7513
Vazan, A., Ormel, C. W., Noack, L., & Dominik, C. 2018, ApJ, 869, 163
Wu, J., Desch, S. J., Schaefer, L., et al. 2018, JGRE, 123, 2691
Xia, X., Weidner, D. J., & Zhao, H. 2015, AmMin, 83, 68
Yagi, T., Suzuki, T., & Akimoto, S.-I. 1985, JGR, 90, 8784
Ye, Y., Prakapenka, V., Meng, Y., & Shim, S. 2017, JGRB, 122, 3450
Zigan, F., & Rothbauer, R. 1967, NJMM, 137, A143